Minerals Engineering 190 (2022) 107935

Contents lists available at ScienceDirect

Minerals Engineering

journal homepage: www.elsevier.com/locate/mineng

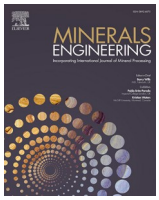

Influence of Co:Fe:Ni ratio on cobalt Pentlandite's electronic structure and surface speciation

Reece R. Waltrovitz [a,b], Gujie Qian [a], Frank de Groot [c], Jamie S. Quinton [a,b], Sarah L. Harmer [a,b,*]

[a] Flinders Microscopy and Microanalysis, Flinders University, Sturt Rd, Bedford Park 5042, South Australia, Australia
[b] Flinders Institute for Nanoscale Science & Technology, Flinders University, Sturt Rd, Bedford Park 5042, South Australia, Australia
[c] Utrecht University, Inorganic Chemistry and Catalysis Group Universiteitsweg 99, 3584 CA Utrecht, The Netherlands

ARTICLE INFO

Keywords:
Pentlandite
XPS
Transition metals
Multiplet effects
Sulfur 2*p* XPS curve fitting
CTM4XAS

ABSTRACT

X-ray photoemission spectroscopy (XPS) was used to investigate the electronic structure and oxidation state of transition metals in synthetic cobalt pentlandites $(Fe,Co,Ni)_9S_8$ with measured stoichiometries of $Fe_{4.85}Ni_{4.64}S_8$, $Co_{0.13}Fe_{4.68}Ni_{4.71}S_8$, $Co_{2.73}Fe_{3.18}Ni_{3.16}S_8$, $Co_{5.80}Fe_{1.63}Ni_{1.59}S_8$ and $Co_{8.70}S_8$. The addition of cobalt was found to decrease the bond length and hence decrease the unit cell dimensions of the cobalt pentlandite crystal structure by up to 0.18 Å. High resolution XPS S 2*p* spectra show increases in the binding energies of bulk 5-coordinated (162.1 eV) and surface 3-coordinated (160.9 eV) sulfur (≈0.2 eV) with increasing Co concentration and decreasing bond lengths. As the Co concentration increases, variation in metal site occupation decreases, resulting in smaller S 2*p* FWHMs due to a dominant single Co-S state rather than mixed Fe-S, Ni-S and Co-S states with similar binding energies. The S 2*p* high binding energy tail, previously identified as a S 3*p*- Fe 3*d* ligand to metal transfer in Fe chalcogenides, shows a marked decrease in intensity as the concentration of Co increases, that is attributed to a decreased probability of ligand-to-metal charge transfer as the e_g orbitals are filled. The transition metal XPS 2*p* spectra were modelled using CTM4XAS to investigate metal site occupation and ligand-to-metal charge transfer. Fe, Co, and Ni were all best simulated using a tetrahedral symmetry and 2+ oxidation state, their $2p_{3/2}$ and $2p_{1/2}$ peaks occurred at 706.9 and 719.9 eV, 778.2 and 793.1 eV, and 852.8 and 870.0 eV, respectively. A negative charge transfer energy confirms the high binding energy tail results from S3*p*-Fe3*d* ligand to metal charge transfer. This increased understanding of the pentlandite electronic structure will provide a basis for the refinement of mineral processing techniques and allow for a reduced environmental impact from limited efficiency.

1. Introduction

Pentlandite $(Fe,Ni)_9S_8$, is an iron-nickel sulfide mined at various sites around the world as the principle nickel ore (Kaneda et al., 1986; Department for Energy and Mining, Nickel, in, Government South Australia, 2020; Pettifer et al., 2020; Kouvo et al., 1959). Mining sites where pentlandites are found, are commonly associated with small percentages of cobalt impurities. The cobalt can occupy metal sites in the pentlandite crystal structure leading to the formation of cobalt pentlandites $(Co,Fe,Ni)_9S_8$ (Department for Energy and Mining, 2020; Kouvo et al., 1959). This cobalt impurity affects the electronic properties and oxidation rates of pentlandite, evident in the varying suitability of cobalt pentlandite for applications such as catalysis (Smialkowski et al., 2021; Al-Mamun et al., 2016; Konkena et al., 2016). An example of the significance of the metal ion ratio is shown in a study done by Smialkowski et al. which demonstrated that the alteration of the metal ion ratios directly influences the electrochemical activation/deactivation behaviour of cobalt pentlandites in catalysis (Smialkowski et al., 2021). Additionally, flotation is directly affected by mineral surface oxidation and coatings which influence the hydrophobicity of the mineral species (Malysiak et al., 2004). This first principles study introduces fitting parameters to further the understanding of the surface chemistry of cobalt pentlandites. This will enable a guide for future studies which attempt to study the variation in surface structure of cobalt pentlandites and optimise applications involving cobalt pentlandites, including floatation and catalysis.

The crystal structure of pentlandite has been well established in literature (Pearson and Buerger, 1956). Pentlandite has a cubic unit cell

* Corresponding author at: GPO Box 2100, Adelaide 5001, South Australia, Australia.
E-mail address: sarah.harmer@flinders.edu.au (S.L. Harmer).

https://doi.org/10.1016/j.mineng.2022.107935
Received 12 July 2022; Received in revised form 16 October 2022; Accepted 11 November 2022
Available online 21 November 2022

with Fm3m symmetry, of which each unit cell contains 36 metal sites which are the focus of this study. The 36 metal sites are split into 32 sites surrounded by a tetrahedral coordination of sulfur atoms, and the remaining 4 which are surrounded by an octahedral coordination of sulfur atoms (Pearson and Buerger, 1956). The 32 sulfur sites are split into 24 "5 coordinate sites" and 8 "4 coordinate sites" which link together metal sites "cube clusters" (Pettifer et al., 2020). A diagram of the unit cell can be seen in Fig. 1.

As pentlandite is an iron-nickel sulfide, the metal sites are commonly shared between iron and nickel, although cobalt, when present, can also occupy these metal sites. Natural pentlandite has no iron- or nickel-rich end members (Fe_9S_8 and Ni_9S_8) as the metal bonds within the pentlandite metal cube clusters become unstable (Vaughan, 1978). This is caused by the 65-electron rule for every base M_9S_8 formula for pentlandite (M representing transition metal ions), where 65 *d*-electrons are shared between the 9 metal sites and the total number of *d* electrons in each tetrahedral site is restricted to seven (Pettifer et al., 2020; Vaughan, 1978). This corresponds to tetrahedral sites that are occupied by Co^{2+} or equal numbers of Fe^{2+} and Ni^{2+} ions (Vaughan, 1978).

The interpretation of transition metal photoemission peaks is often complicated due to overlapping bulk and surface states, and multiplet effects that further complicate the accurate assignment of components. The influence of cobalt on the photoemission spectra of pentlandite has been scarcely reported. Previous studies on pentlandite have focussed on the states of the iron and nickel occupying the metal sites. Pettifer et al. used synchrotron X-ray photoelectron spectroscopy (SXPS) to investigate the Fe, Ni, and S 2*p* peaks of pentlandite. This study, like several similar, was completed without the presence of cobalt impurities (Pettifer et al., 2020; Mkhonto et al., 2015; Legrand et al., 1997; Legrand et al., 2005). Similar studies have been concerned with the mechanisms associated with surface oxidation and identification of surface oxidation products using the Fe, Ni, and S XPS 2*p* peaks. A study by Legrand et al. found that pentlandite sample surfaces oxidise rapidly and form an "overlayer" comprising of Fe(III)-S, Fe(III)-O, $Ni(OH)_2$, and $NiSO_4$ (Legrand et al., 2005). This overlayer was dominated by iron oxides and sulfides suggesting that iron oxidises preferentially over nickel (Pettifer et al., 2020; Richardson and Vaughan, 1989). Additionally, in these studies, XPS was used to determine bulk and surface speciation Pettifer et al. found that the bulk pentlandite included 4- and 5-coordinated sulfur with XPS $2p_{3/2}$binding energies of 161.7 eV and 162.2 eV, respectively. Upon fracture, each sulfur lost a bonding partner and XPS showed evidence of 3- and 4-coordinate sulfur corresponding to $2p_{3/2}$ binding energies of 161.1 eV and 161.7 eV, respectively (Pettifer et al., 2020). Finally, Pettifer et al. and Richardson and Vaughn, found that the bulk iron was in the form of Fe(II)-S with an Fe $2p_{3/2}$ peak centred at 707.3 eV (Pettifer et al., 2020; Richardson and Vaughan, 1989). The Ni $2p_{3/2}$ peak resides at 852.77 eV in agreement with Pettifer et al. proposing it at 852.8 eV and Legrand et al (Pettifer et al., 2020; Legrand et al., 2005). The location of this peak indicates bulk nickel in the form of Ni(II)-S (Pettifer et al., 2020; Richardson and Vaughan, 1989).

Few studies have investigated cobalt pentlandites experimentally, Al-Mamun et al. analysed the Co 2*p* lines of cobalt pentlandites which displayed two sets of doublets. The $2p_{1/2}$ and $2p_{3/2}$ peaks occurred at energies of 779.5 eV and 795.4 eV, respectively for the first set. The second set displayed $2p_{1/2}$ and $2p_{3/2}$ peaks at energies of 781.0 eV and 796.7 eV, respectively (Al-Mamun et al., 2016). However, spectra displayed showed great signs of sample oxidation which would have altered the electronic structure of the material.

Simulations and measurements of high-resolution XPS spectra are required to understand the multiplet effects that complicate transition metal 2*p* photoemission spectra from high spin states (Biesinger et al., 2011). This has been attempted using Density Functional Theory (DFT) calculations, although these are flawed as they commonly do not allow for excited state calculations (de Groot, 2005). DFT calculations are computationally difficult for large structures so simplified models must be chosen (Mkhonto et al., 2015; Burdett and Miller, 1987; Hoffman et al., 1990). DFT calculations also cannot account for the overlap between the core and valence electron wavefunctions, which causes atomic multiplet splitting (de Groot, 2005). Studies by Stentine et al. and Ramanantoanina and Daul have used modified DFT methods, which include ligand-field theory, to successfully calculate 3d transition metal 2*p* core electron binding energies (Ramanantoanina and Daul, 2017; Stetina et al., 2019). In comparison to DFT, CTM4XAS is a more simplistic method based on the charge transfer multiplet effects. The development of CTM4XAS was based around the initial and final state effects, allowing accurate simulation of the core 2*p* electron binding energies of transition metals (Stavitski and de Groot, 2010). The reliability of CTM4XAS makes it the best choice for simulating the core electron binding energies for the transition metals present in pentlandite (Stavitski and de Groot, 2010).

This study aims to identify the changes in chemical states with the addition of cobalt and determine whether there is any preferential occupation of metal sites. High resolution X-ray photoelectron spectroscopy has been used on vacuum-fractured synthetic pentlandite samples to distinguish the discrete change in chemical states. This is then compared with CTM4XAS simulations to determine what chemical states dominate the photoemission spectra and to which sites they correspond.

2. Methods

2.1. Sample synthesis

Pentlandite (M_9S_8) samples with stoichiometries of $Fe_{4.85}Ni_{4.64}S_8$,

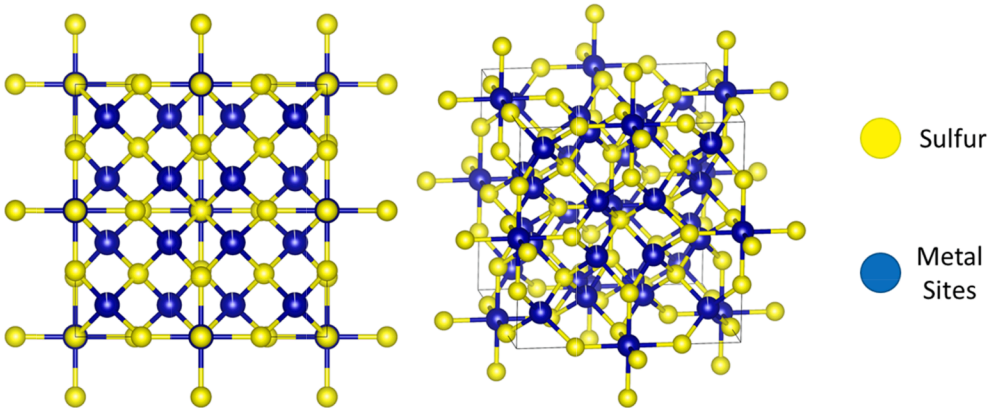

Fig. 1. Crystal structure of pentlandite; containing 32 tetrahedral and 4 octahedral metal sites per unit cell. Metal sites can be occupied by either Fe, Ni or Co (Momma and Izumi, 2011).

$Co_{0.13}Fe_{4.68}Ni_{4.71}S_8$, $Co_{2.73}Fe_{3.18}Ni_{3.16}S_8$, $Co_{5.80}Fe_{1.63}Ni_{1.59}S_8$ and $Co_{8.70}S_8$ were synthesised with cobalt powder (<150μ m, 99.9+% Sigma-Aldrich), iron wire (1.0 mm diameter, 99.9+%, Sigma-Aldrich), nickel wire (0.5 mm diameter, 99.9+%, Sigma-Aldrich) and sulfur flakes (99.99+%, Sigma-Aldrich), using the standard silica tube method (Vaughan, 1978). Stoichiometries were confirmed by the Flinders University CSE Chemical Analysis Services team with inductively coupled plasma optical emission spectroscopy (ICP-OES) see Fig 2. The materials were sealed inside evacuated silica tubes ($<10^{-2}$ Torr) and heated in a furnace from ambient temperature to 445 °C, held for 3 h, then ramped to 700 °C and held for 3 h, and finally ramped to 1150 °C and held for 11 h. The furnace was then turned off as the sample cooled to room temperature. All heating stages increased at a rate of 1 °C/min and samples were limited to a size of 2 g to prevent tube failure. This is modified from previously published procedures to increase homogeneity of the samples (Pettifer et al., 2020; Xia et al., 2008).

2.2. Data acquisition

Powder X-ray Diffraction (PXRD) analysis was carried out at Flinders Microscopy and Microanalysis (Flinders University) using a Bruker D8 Advance Eco Powder X-Ray Diffractometer with a Co Kα radiation source ($\lambda = 1.7902$Å). Prior to PXRD, samples were sanded alongside the outer edges to remove any iron sulfide, cobalt sulfide or nickel sulfide phases which form during the synthesis process. Samples were then ground to a particle size of < 50 μm using a quartz mortar and pestle. This powder was evenly spread on a zero-background silicon substrate disc and placed into the sample holder. XRD data were all collected across the 2θ range of 10 to 90° with a step size of 0.02° and 0.5 s per step. Qualitative analysis of samples was completed using Diffrac.EVA where spectra were matched with reference spectra from the Crystallography Open Database (COD). Diffrac.TOPAS was used to calculate unit cell dimensions.

X-ray photoelectron spectra were collected using a Kratos AXIS Ultra DLD spectrometer with a monochromatic Al Kα radiation source (1486.6 eV, 225 W, 15 kV, 15 mA). The spectrometer was calibrated to give Au $4f_{7/2}$ and Cu $2p_{3/2}$ binding energies of 84.03 eV and 932.69 eV, respectively. All spectra were collected over a rectangular analysis area with dimensions 300 × 700 μm. Spectra were charge corrected by standard protocols with the C1s adventitious carbon peak of 248.8 eV (Johansson et al., 1973; Biesinger, 2022). As the sampling depth of XPS is within the order of several nm, it was crucial to obtain a pristine surface for analysis. Samples were, therefore, initially loaded into a nitrogen-filled glovebox. They were then cleaved with cutters, mounted onto copper stubs, and immediately transferred into the analysis chamber. The samples were then transferred to the analysis chamber where the pressure was maintained at $< 3 \times 10^{-8}$ Torr during analysis.

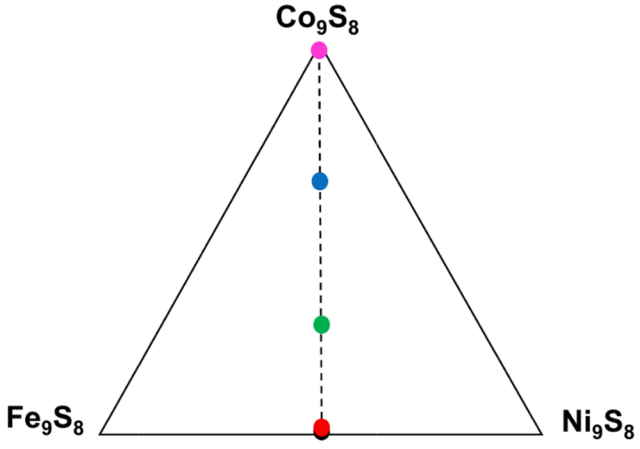

Fig. 2. Pentlandite compositions synthesised in this study to investigate electronic structure changes with Co.

Survey spectra were collected with a pass energy of 160 eV, step size of 0.5 eV. C 1 *s* and O 1 s spectra were collected with a pass energy of 20 eV and a step size of 0.1 eV. S 2*p* spectra were collected with a pass energy of 10 eV and a step size of 0.025 eV, while 2*p* spectra for transition metals (Fe, Ni and Co) were collected with a pass energy of 20 eV and a step size of 0.05 eV.

The XPS spectra were processed using CasaXPS software (Fairley, 2010). All spectra were fitted using a Shirley background and normalised to bulk signal to allow comparison between spectra (Shirley, 1972). Each sulfur spectrum was fitted with a doublet separated by 1.19 eV with equal full width half maximums (FWHM) and an area ratio of 2:1 for $2p_{3/2}$:$2p_{1/2}$. A tail shape (fitted with three, GL(50) peaks) due to ligand to metal charge transfer is fitted relative to the bulk 5 coordinated sulfur as per Pettifer et al. (Pettifer et al., 2020).

Charge transfer multiplets for X-ray absorption spectroscopy (CTM4XAS) is software which has been developed for the simulation of transition metal core level photoemission spectra, and details of its scope and operational parameters have been previously reported by Stavitski (Stavitski and de Groot, 2010). In this work, CTM4XAS has been used to simulate transition metal 2*p* spectra and compare changes between them for metals with the addition of cobalt. The oxidation state was set to divalent for Fe, Co and Ni simulations, as pentlandite transition metal spectra have previously had main peaks assigned to Fe(II)-S and Ni(II)-S contributions (Pettifer et al., 2020; Legrand et al., 2005). Slater integral reduction values, F_{dd}, F_{pd} and G_{pd}, were altered slightly from 1 for optimal fit, with the value of 1 representing atomic parameters calculated within the Hartree-Fock limit (Stavitski and de Groot, 2010). The spin–orbit parameters are defined for the program by Stavitski and de Groot; core spin–orbit coupling is not usually screened and should always be set to the default value of 1 whereas valence spin-orbit coupling has been found to alternate between 0 and 1 depending on the 3d transition metal system (Stavitski and de Groot, 2010). A valence spin-orbit coupling value of 0 was found to model this series of cobalt pentlandites most accurately. Crystal field parameters were chosen to represent the symmetry and crystal field splitting at the metal site, as pentlandite is dominated by tetrahedral metal sites. In addition, simulations were set with an octahedral symmetry and negative 10Dq value to simulate a tetrahedral coordination (Stavitski and de Groot, 2010). Finally, charge transfer parameters were employed to describe the charge transfer effect (De Groot and Kotani, 2008). The charge transfer energy, Δ, gives the energy difference between $3d^n$ and $3d^{n+1}L$ states. U_{dd} and U_{pd} values define the Hubbard U value and core hole potential, respectively. $T(e_g)$ and $T(t_{2g})$ define the hopping parameters for the two groups of orbitals (Stavitski and de Groot, 2010). For simulations the charge parameters were iteratively changed to provide the best fit with a constraint of U_{pd} being fixed at 1–2 eV larger than U (Ikeno et al., 2009).

3. Results

3.1. 1. X-Ray diffraction

PXRD data for the two $Fe_{4.85}Ni_{4.64}S_8$ and $Co_{8.70}S_8$ end-member samples are shown in Fig. 3. Measured spectra were matched with reference spectra from the COD database (Tsukimura et al., 1992). A strong correlation is observed between diffraction spectra and the reference pattern. Comparison shows an increase in 2Θ from reference patterns with the addition of cobalt. This has previously been observed where it was witnessed that the unit cell dimensions decrease with the addition of cobalt, causing the spectra to peak shift (Kouvo et al., 1959; Rajamani and Prewitt, 1975). Calculated unit cell dimensions are shown in Table 1. The unit cell dimension was found to decrease by 0.18 Å across the series from $Fe_{4.85}Ni_{4.64}S_8$ to $Co_{8.70}S_8$, in agreement with previous findings that the unit cell of pentlandite decreases with increasing Co concentration (Kouvo et al., 1959; Rajamani and Prewitt, 1975). This decrease in the unit cell dimension is caused by an

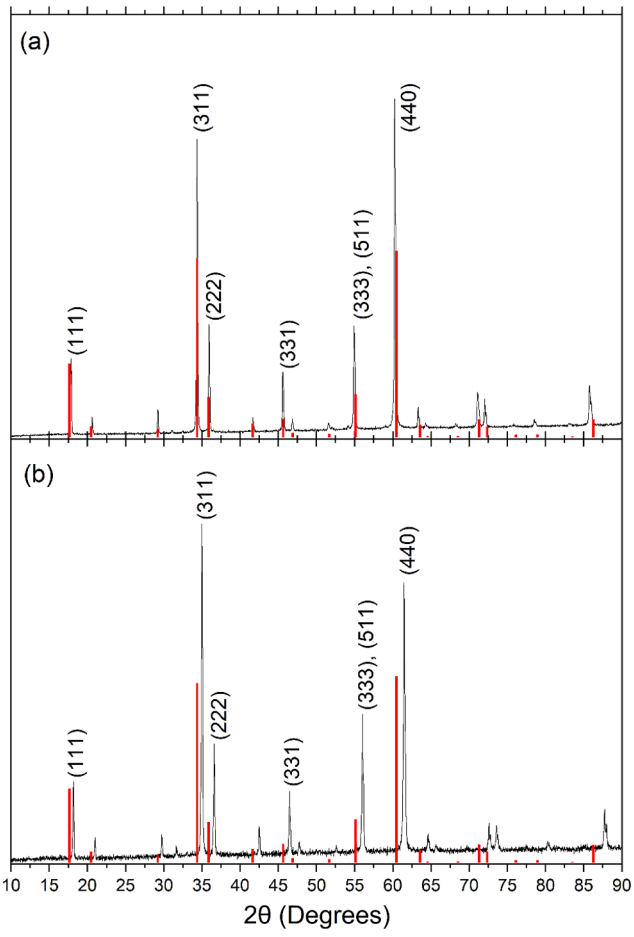

Fig. 3. X-ray diffraction (XRD) spectra for (a) $Fe_{4.85}Ni_{4.64}S_8$ and (b) $Co_{8.70}S_8$ compared to pentlandite reference patterns (red). This highlights the contraction of the unit cell with the increase in Co. (For interpretation of the references to colour in this figure legend, the reader is referred to the web version of this article.)

Table 1
Summary of ICP-OES analysis for all pentlandite samples.

Sample Name	Co 228.616 (mg/g sample)	Fe 259.939 (mg/g sample)	Ni 221.648 (mg/g sample)	S 180.669 (mg/g sample))
$Fe_{4.85}Ni_{4.64}S_8$	<LOQ	322.032	323.825	305.097
$Co_{0.13}Fe_{4.68}Ni_{4.71}S_8$	9.349	321.765	340.370	315.605
$Co_{2.73}Fe_{3.18}Ni_{3.16}S_8$	200.368	221.327	231.060	319.490
$Co_{5.80}Fe_{1.63}Ni_{1.59}S_8$	406.222	108.115	111.012	305.068
$Co_{8.70}S_8$	622.565	<LOQ	<LOQ	311.511

increasing electronegativity as the covalence of metal and ionic bonds increases with the addition of Co and hence bond lengths decrease.

3.2. XPs

3.2.1. Survey XPS spectra

Survey spectra for all pentlandite samples are shown in Fig. 4, with the resultant quantification in Table 2. The metal:sulfur ratio decreases significantly for $Co_{2.73}Fe_{3.18}Ni_{3.16}S_8$ and $Co_{5.80}Fe_{1.63}Ni_{1.59}S_8$ samples. Overlap between the transition metal peaks used for quantification may have caused an over-measured background to be fit and reduced the amount detected through quantification. The survey and high-resolution scans indicate adventitious carbon and oxygen species have formed

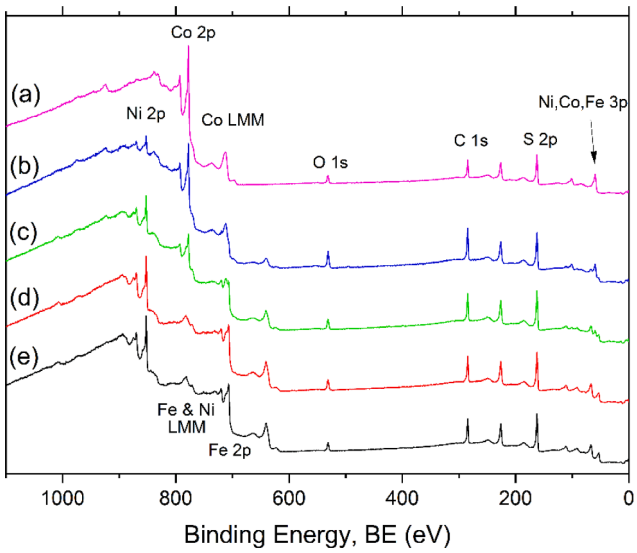

Fig. 4. Survey XPS spectra of pentlandite samples; (a) $Co_{8.70}S_8$, (b) $Co_{5.80}Fe_{1.63}Ni_{1.59}S_8$, (c) $Co_{2.73}Fe_{3.18}Ni_{3.16}S_8$, (d) $Co_{0.13}Fe_{4.68}Ni_{4.71}S_8$, and (e) $Fe_{4.85}Ni_{4.64}S_8$. Significant peaks are labelled with the corresponding photoemission they represent.

during sample preparation. There is also evidence to suggest oxidation with the oxygen concentration varying between 6.8 and 12.22 at.%. The oxygen peaks were investigated in more detail with high-resolution O 1 *s* scans (see Section 3.2.2). To briefly summarise, analysis of O 1 *s* and S 2*p*, has shown that no sulfur oxy species are present and although the Fe 2*p* spectra can be seen to be highly oxidised, it has not influenced the sample beyond this.

3.2.2. Oxygen 1s XPS spectra

The O 1 s spectra display a main peak centred around 531.8 eV, resulting primarily from hydroxides at the pentlandite surface (Fig. 5 and Table 3). Hydroxides have commonly been linked to the preferential oxidation of Fe in pentlandite (Legrand et al., 2005). As this remains largely constant between all samples, it may suggest that Co and Fe undergo oxidation at a similar rate. A shoulder observed at approximately 530.1 eV, has been assigned to a combination of O^{2-} and OH^-. Increasing the cobalt ratio favours the formation of OH^- over O^{2-} masking the presence of this shoulder. The oxygen contribution from sulfates was not included as the high-resolution sulfur spectra show no signs of sulfates (Section 3.3.3), indicative of the absence of major surface alteration due to oxidation.

3.2.3. Sulfur 2p XPS spectra

Sulfur 2*p* XPS spectra collected are shown in Fig. 6 along with fitting parameters presented in Table 4. $Fe_{4.85}Ni_{4.64}S_8$ XPS spectra have previously been well discussed by Pettifer et al. and Legrand et al. (Pettifer et al., 2020; Legrand et al., 1997; Legrand et al., 2005). Two main features are evident at approximately 162.2 eV and 163.4 eV corresponding to the main $2p_{3/2}$ and $2p_{1/2}$ peaks from pentlandite which have been attributed to bulk fully coordinated monosulfide (Pettifer et al., 2020; Legrand et al., 2005). The peak shows a slight asymmetry to high binding energy with an energy loss tail that extends to 168 eV (Pettifer et al., 2020). The absence of features between 166 eV and 170 eV confirms the absence of sulfur oxy species. A low binding energy shoulder was observed at 161.7 eV. This shoulder has been attributed by Pettifer et al. as a combination of bulk/surface 4-coordinated sulfur and surface 3-coordinated sulfur with small surface contributions (<10 at.%) to the XPS spectra at photon energies of > 1000 eV (Pettifer et al., 2020). The residuals for the S 2*p* fits displayed in Fig. 6 showed no indication of doublet structures at 1.19 eV apart as expected for S. This suggests no

Table 2
Unit Cell Dimensions measured for Synthetic Pentlandite Samples from XRD spectra.

	$Fe_{4.85}Ni_{4.64}S_8$	$Co_{0.13}Fe_{4.68}Ni_{4.71}S_8$	$Co_{2.73}Fe_{3.18}Ni_{3.16}S_8$	$Co_{5.80}Fe_{1.63}Ni_{1.59}S_8$	$Co_{8.70}S_8$
Unit Cell Dimension, a (Å)	10.04	10.04	9.97	9.92	9.86

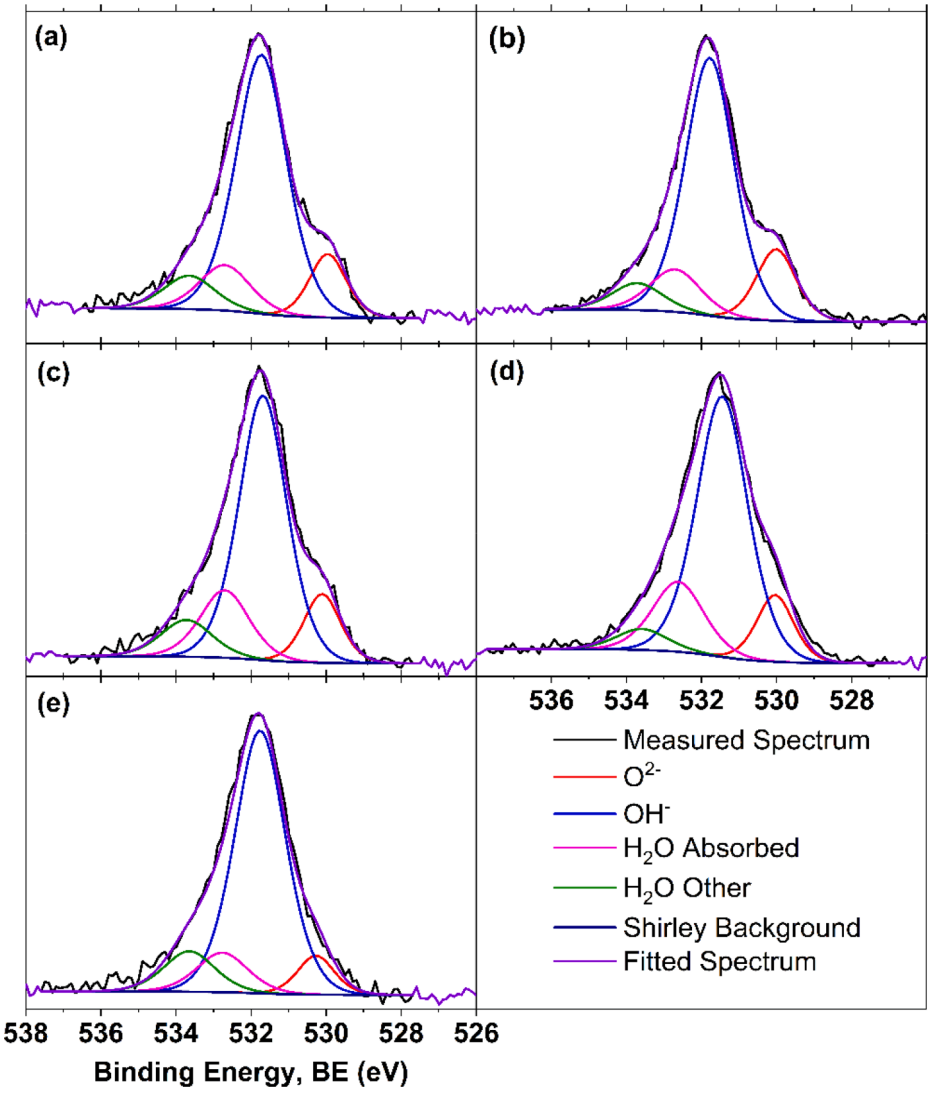

Fig. 5. Oxygen 1*s* XPS spectra collected from: (a) $Fe_{4.85}Ni_{4.64}S_8$, (b) $Co_{0.13}Fe_{4.68}Ni_{4.71}S_8$, (c) $Co_{2.73}Fe_{3.18}Ni_{3.16}S_8$, (d) $Co_{5.80}Fe_{1.63}Ni_{1.59}S_8$ and (e) $Co_{8.70}S_8$ with fits for O^{2-}, OH^-, and H_2O components.

Table 3
Quantification results of XPS spectra from Fig. 4. The metal:sulfur ratio has been calculated to display transition metal sensitivity that has been lost due to the background.

Target Stoichiometry	XPS Quantification Results						Metal: Sulfur Molar ratio
	Co at. %	Fe at. %	Ni at. %	S at. %	C at. %	O at. %	
$Fe_{4.85}Ni_{4.64}S_8$	0.0	8.6	11.2	33.6	39.7	6.8	4.7: 8
$Co_{0.13}Fe_{4.68}Ni_{4.71}S_8$	0.0	8.5	10.6	33.7	39.7	7.5	4.5: 8
$Co_{2.73}Fe_{3.18}Ni_{3.16}S_8$	2.3	3.2	5.5	37.5	43.5	8.0	2.3: 8
$Co_{5.80}Fe_{1.63}Ni_{1.59}S_8$	7.2	0.7	1.6	31.6	46.6	12.2	2.4: 8
$Co_{8.70}S_8$	23.8	0.0	0.0	34.4	34.1	7.7	5.5: 8

other sulfur or sulfur-oxy species is present. Thus, the asymmetric high binding energy tail has been fit and linked to the 5-coordinate sulfur as described previously by Pettifer et al. (Pettifer et al., 2020).

As the Co concentration increases from $Fe_{4.85}Ni_{4.64}S_8$ (0 wt%) to $Co_{8.70}S_8$ (66.7 wt%), there is a notable ~ 0.2 eV increase in binding energy to the 5-coordinated and 3-coordinated sulfur contributions, except for $Co_{0.13}Fe_{4.68}Ni_{4.71}S_8$. This is due to the decreasing unit cell dimensions with increasing cobalt content. Furthermore, this suggests that there is a link between the 5-coordinated and 3-coordinated sites and that upon fracture the 5-coordinated sulfur is likely to lose two bonding partners. Contributions from the 4-coordinated sulfur were found to increase by 0.07 eV across the series, a much smaller increase compared to the 5-coordinated and 3-coordinated sites. The combined increase in the binding energy observed is a result of the decreasing bond lengths and the decreasing unit cell dimension. Another result of

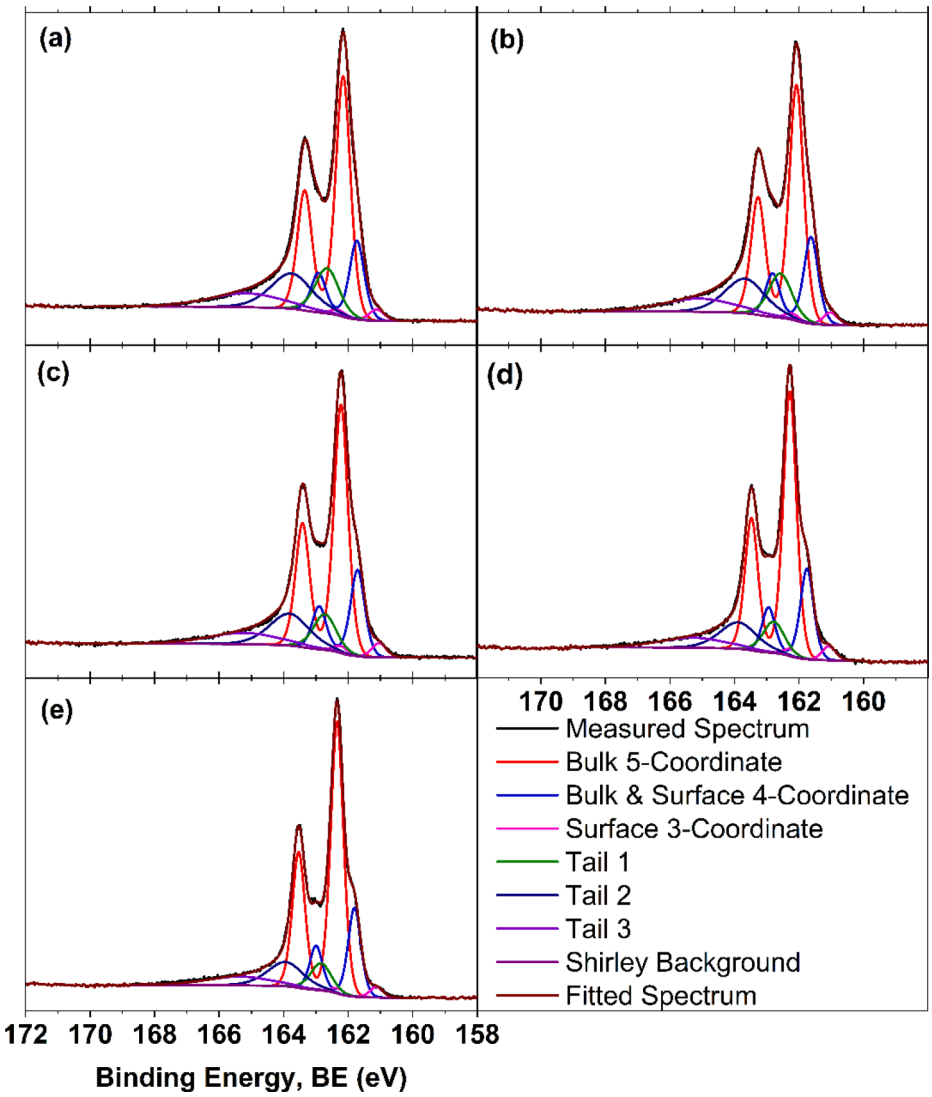

Fig. 6. Sulfur 2*p* XPS spectra collected from (a) $Fe_{4.85}Ni_{4.64}S_8$, (b) $Co_{0.13}Fe_{4.68}Ni_{4.71}S_8$, (c) $Co_{2.73}Fe_{3.18}Ni_{3.16}S_8$, (d) $Co_{5.80}Fe_{1.63}Ni_{1.59}S_8$ and (e) $Co_{8.70}S_8$ with 5, 4 and 3-coordinate fits and their associated ligand to metal charge transfer tails..

Table 4
Fitting parameters for components displayed in Fig. 5, fit to the O 1*s* XPS Spectra.

Species	$Fe_{4.85}Ni_{4.64}S_8$	$Co_{0.13}Fe_{4.68}Ni_{4.71}S_8$	$Co_{2.73}Fe_{3.18}Ni_{3.16}S_8$	$Co_{5.80}Fe_{1.63}Ni_{1.59}S_8$	$Co_{8.70}S_8$
O^{2-} at.% (FWHM = 1.15 eV) (530.1 ± 0.2 eV)	0.8	1.0	1.0	1.5	0.6
OH^- at.% (FWHM = 1.6 eV) (531.6 ± 0.2 eV)	4.6	5.1	5.1	8.0	5.5
H_2O Absorbed at.% (FWHM = 1.6 eV) (532.7 ± 0.1 eV)	0.8	0.8	1.2	2.1	0.8
H_2O Other at.% (FWHM = 1.6 eV) (533.7 ± 0.1 eV)	0.6	0.5	0.7	0.6	0.8
Total O at.%	6.8	7.5	8	12.2	7.7

the increasing Co ratio is a deepening in the valley between the $2p_{3/2}$ and $2p_{1/2}$ peaks as well as a decrease to the high binding energy tail. The fit contributions for these areas are dominated by the peaks fitted for the tail shape as per Pettifer et al. (Pettifer et al., 2020). The tail area proportional to the bulk 5-coordinated component had to be altered to allow for the best fit (Table 5). All tail components, resulting from the ligand to metal charge transfer, were found to decrease with increasing Co content, suggesting that the presence of cobalt reduces the likelihood of the ligand to metal charge transfer. This can be explained considering the valence orbitals of iron and cobalt present predominantly as tetrahedral coordinations in the pentlandite. For divalent iron and cobalt in a tetrahedral coordination, the e_g set of 3*d* orbitals are more deeply bound

Table 5
Fitting parameters for components displayed in Fig. 6, fit to the S 2*p* XPS Spectra.

	$Fe_{4.85}Ni_{4.64}S_8$	$Co_{0.13}Fe_{4.68}Ni_{4.71}S_8$	$Co_{2.73}Fe_{3.18}Ni_{3.16}S_8$	$Co_{5.80}Fe_{1.63}Ni_{1.59}S_8$	$Co_{8.70}S_8$
FWHM (eV)	0.54	0.53	0.52	0.48	0.47
5-Coordinated					
Binding Energy (eV)	162.16	162.08	162.22	162.28	162.34
% Contribution	49.0	48.0	51.2	54.4	57.3
4-Coordinated					
Binding Energy (eV)	161.73	161.63	161.71	161.75	161.8
% Contribution	16.1	17.7	17.8	18.6	18.7
3-Coordinated					
Binding Energy (eV)	160.92	161.02	161.04	161.07	161.13
% Contribution	2.3	2.5	2.9	3.0	2.3
Total S%	33.6	33.7	37.5	31.6	34.4

compared to the t_{2g} set. These e_g orbitals are filled for divalent cobalt whereas for divalent iron they require an extra electron. Therefore, the ligand-to-metal charge transfer is more likely to occur for iron and consequently fills the e_g orbitals (Vaughan, 1978).

3.2.4. Iron 2p XPS spectra

Iron 2*p* XPS spectra collected from pentlandite samples $Fe_{4.85}Ni_{4.64}S_8$, $Co_{0.13}Fe_{4.68}Ni_{4.71}S_8$, $Co_{2.73}Fe_{3.18}Ni_{3.16}S_8$, and $Co_{5.80}Fe_{1.63}Ni_{1.59}S_8$, are shown in Fig. 7. Each spectrum displays two main peaks at 706.9 eV and 719.9 eV corresponding to the $2p_{3/2}$ and $2p_{1/2}$ photoemission peaks, respectively. The $2p_{3/2}$ peak energy is consistent with divalent iron previously reported at 707.3 eV and 706.75 eV, respectively (Pettifer et al., 2020; Legrand et al., 1997). The broad nature of the peak is due to multiplet splitting of high-spin divalent iron. Note: low-spin divalent iron does not experience multiplet splitting as all valence electrons are paired. A broad feature at 712.5 eV is evident in the $Fe_{4.85}Ni_{4.64}S_8$ sample and increases in intensity with the addition of cobalt. This shows that there are two components for this feature; in sample $Fe_{4.85}Ni_{4.64}S_8$ this is due to an underlying Ni LMM Auger at 712 eV (Moulder, 1995). As the cobalt content in the sample increases, this feature becomes dominant, due to the presence of a Co LMM Auger line at 713 eV (Moulder, 1995). There is no visible evidence of changes between spectra with the addition of cobalt.

CTM4XAS simulations were performed to best fit the binding energy difference between the $2p_{3/2}$ and $2p_{1/2}$ peaks due to spin–orbit coupling as well as the multiplet structure at the high binding energy side of the bulk peaks. Simulation parameters are shown in Table 6. The main parameters for the transition metals are the oxidation state, crystal field splitting (10Dq), and the charge transfer energy (Δ). The iron 2*p* spectrum was best simulated with a 2 + oxidation state and a 10Dq value of −1.5, which shows that the simulation matches best with a tetrahedral metal site coordination. Finally, Δ = 2 indicates a lower energy ground initial state as compared to the ligand to metal charge transfer initial state. The simulated spectrum was found to match the measured peaks quite closely, although peak broadening between 710 eV and 715 eV could not be accurately simulated (Fig. 8). The iron 2*p* spectra have contributions from a large inelastically scattered electron background. As a result, the Shirley background often produces a poor fit between the $2p_{3/2}$ and $2p_{1/2}$. This difficulty in fitting the region between 710 eV and 715 eV is more challenging in the presence of oxidation products. Iron has been found to preferentially oxidise in pentlandite, forming oxide and hydroxide products between 709 and 711 eV, respectively, partially contributing to the difference observed between simulated and measured spectra (Legrand et al., 2005).

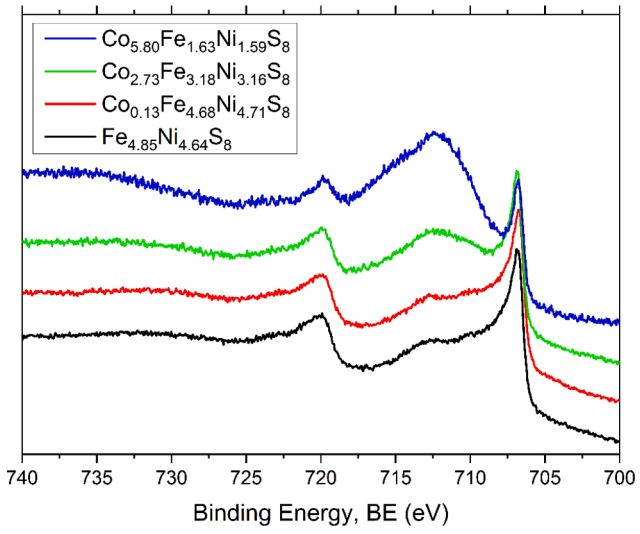

Fig. 7. Fe 2*p* XPS spectra of fractured pentlandite and cobalt pentlandites.

3.2.5. Cobalt 2p XPS spectra

The cobalt 2*p* XPS spectra for pentlandite samples are shown in Fig. 9. Two main Co^{2+} peaks at 778.2 eV and 793.1 eV, corresponding to Co $2p_{3/2}$ and $2p_{1}/2$, were observed in samples $Co_{2.73}Fe_{3.18}Ni_{3.16}S_8$, $Co_{5.80}Fe_{1.63}Ni_{1.59}S_8$ and $Co_{8.70}S_8$. There has been limited research published regarding the Co 2*p* spectra for cobalt pentlandites. Al-Mamun et al. synthesised cobalt pentlandite for examination of evolution of oxygen species during reactions using XPS. The Co 2p lines were fit with two sets of doublets with $2p_{3/2}$ energies of 779.5 eV and 781.0 eV and $2p_{1/2}$ energies of 795.4 eV and 796.7 eV, respectively (Al-Mamun et al., 2016). The survey scan for this sample showed large amounts of oxidation as indicated by a very prominent O 1 *s* peak. A comparison between this study and the work by Al-Mamun (2016) suggests that: (1) the doublet at 779.5 eV and 795.4 eV in Al-Mamun (2016) (at 778.2 eV and 793.1 eV, respectively, in the present study) is most likely from the pristine cobalt pentlandite; and (2) the other doublet at 781.0 eV and 796.7 eV is possibly due to Co oxidation.

The Co 2p XPS spectra collected on vacuum-fractured samples $Fe_{4.85}Ni_{4.64}S_8$ and $Co_{0.13}Fe_{4.68}Ni_{4.71}S_8$ display the dominant broad feature at 782.2 eV and a smaller feature at 771.6 eV. Their energies coincide with the Fe and Ni LMM Auger peaks at 784 eV and 772 eV, respectively, for an Al X-ray source (Moulder, 1995). The Auger peaks are present in samples $Co_{2.73}Fe_{3.18}Ni_{3.16}S_8$ and $Co_{5.80}Fe_{1.63}Ni_{1.59}S_8$ as a slight addition to the multiplet structure. An attempt to remove the Auger emission lines was achieved by fitting the Co 2p spectrum of sample $Fe_{4.85}Ni_{4.64}S_8$ with a general line shape representing the Auger emissions and adjusting for the varying concentrations of Fe and Ni. There are no changes observable in the spectra for samples $Co_{2.73}Fe_{3.18}Ni_{3.16}S_8$, $Co_{5.80}Fe_{1.63}Ni_{1.59}S_8$ and $Co_{8.70}S_8$ with the addition of cobalt, suggesting that the chemical state of Co does not change greatly with metal ratios.

The Co 2*p* spectra simulated using CTM4XAS and a range of parameters (Table 7) are presented in Fig. 10. A 2+ oxidation state was chosen to align with the 65-electron rule for pentlandite and a 10Dq value of −1.5 to simulate a tetrahedral metal site coordination. In addition, a Δ value of −2.5 was applied to represent a lower energy

Table 6
Sulfur 2p high binding energy tail area relative to the bulk 5-coordiante sulfur component.

	$Fe_{4.85}Ni_{4.64}S_8$	$Co_{0.13}Fe_{4.68}Ni_{4.71}S_8$	$Co_{2.73}Fe_{3.18}Ni_{3.16}S_8$	$Co_{5.80}Fe_{1.63}Ni_{1.59}S_8$	$Co_{8.70}S_8$
Tail Area					
Tail 1	× 0.3	× 0.3	× 0.23	× 0.19	× 0.16
Tail 2	× 0.41	× 0.41	× 0.36	× 0.28	× 0.25
Tail 3	× 0.29	× 0.28	× 0.23	× 0.19	× 0.16

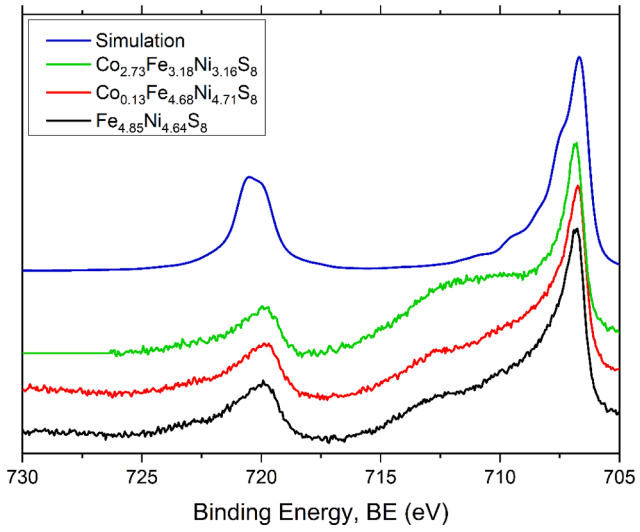

Fig. 8. Fe 2*p* XPS spectra from pentlandite, cobalt pentlandites in comparison to simulated high spin Fe 2p XPS spectra.

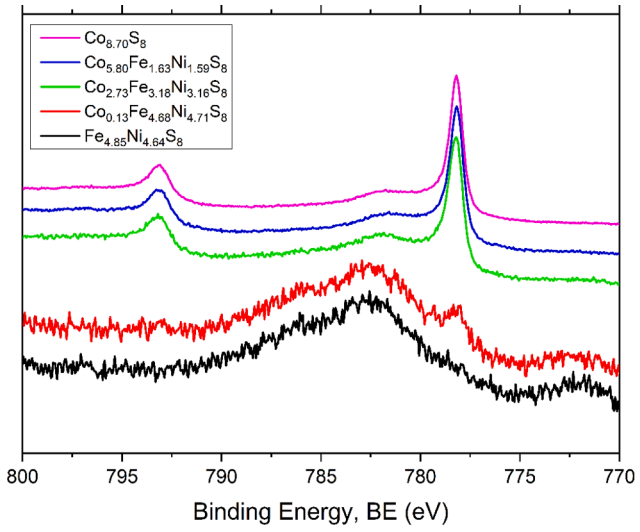

Fig. 9. Co 2p XPS spectra of fractured pentlandite and cobalt pentlandites.

charge transfer initial state. Simulated and experimental peak positions are matched very closely although the broadening of the $2p_{3/2}$ peak is slightly over simulated. There are also two simulated features at 787 eV which is not evident in experimental data. These features were necessary to match the multiplet structure most accurately at 781 eV. The peak separation in simulated data is slightly greater than measured, this could be fixed by decreasing the core spin–orbit coupling value although, although this is not usually screened and should always be set to 1 (Section 2.2) (Stavitski and de Groot, 2010).

3.3. Nickel 2p XPS spectra

Nickel 2*p* XPS spectra, shown in Fig. 11 alongside the simulated spectrum, have a strong $2p_{3/2}$ peak at 852.8 eV and a $2p_{1/2}$ peak at 870.0 eV. The peak assignment agrees with previous studies by Pettifer et al. and Legrand et al. who reported the Ni $2p_{3/2}$ peak at 852.8 and 852.77 eV, respectively for Ni(II)-S (Pettifer et al., 2020; Legrand et al., 2005). There is a broad shake-up satellite peak at 858.77 eV (Legrand et al., 1997). It also appears that there is a small feature at around 856 eV, suggesting the presence of nickel hydroxide species due to oxidation on the sample surface (Legrand et al., 1997). It was also found that the Ni 2*p* spectra did not change with the addition of cobalt, suggesting similar chemical states between samples, or the changes are not visible due to the broad nature of the peak.

The simulation parameters are shown in Table 8. An oxidation state of 2 + and a 10Dq value of −1 were chosen to follow the 65-electron rule and tetrahedral metal site dominant crystal structure. A Δ of 2 indicates a lower energy ground initial state. The correlation between the simulated and measured spectra is very high for Ni. The line shapes of both $2p_{3/2}$ and $2p_{1/2}$ are in great agreement although again peak separation is slightly greater than measured (see Table 9).

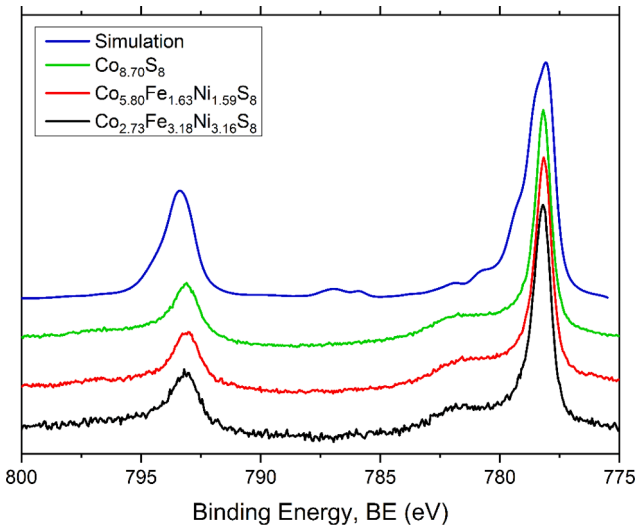

Fig. 10. Co 2*p* XPS spectra from pentlandite, cobalt pentlandites in comparison to simulated high spin Co 2*p* XPS spectra.

Table 7
Fe 2p Simulation parameters used in CTM4XAS to provide the highest accuracy simulations.

	Slater Integral Reduction			Spin-Orbit Coupling Reduction		Crystal Field Parameters	Charge Transfer Parameters				
Spectra	F_{dd}	F_{pd}	G_{pd}	Core	Valence	10Dq (O_h)	Δ	U_{dd}	U_{pd}	$T(e_g)$	$T(t_{2g})$
Fe(II) 2*p*	1	1	0.8	1	1	−1.5	2	4	5	1.5	3

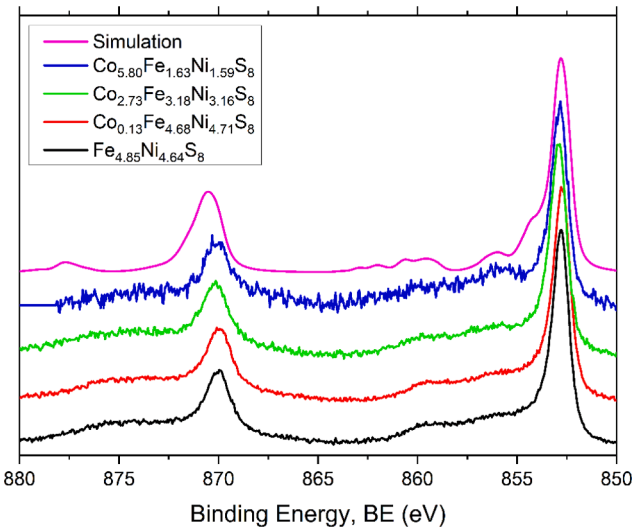

Fig. 11. Ni 2*p* XPS spectra from pentlandite, cobalt pentlandites in comparison to simulated high spin Ni 2p XPS spectra.

4. Discussion

4.1. Metal site occupation

Synthetic pentlandites have been suggested to exhibit tetrahedral and octahedral sites each occupied by an equal number of each transition metal (Tenailleau et al., 2006), whereas natural pentlandite has shown a preferential filling for Fe^{2+} on the octahedral sites (Tsukimura et al., 1992). The implications of adding cobalt into pentlandite have not been explored to date. XPS spectra for 3d transition metals were used to explore possible changes in chemical state and hence potential for a change in metal site ordering. Fe and Ni 2*p* XPS spectra both showed no apparent changes in chemical states as a function of Co concentration, suggesting that there is no change in the oxidation state or co-ordination of the metal ions in the lattice. Therefore, with the addition of Co it appears that ordering continues to occur randomly for synthetic pentlandites with an equal number of Fe and Ni present at each metal site.

It remains unclear whether there is any preferential site occupation for Co in the pentlandite crystal structure. The Co 2*p* XPS spectra again show no clear changes in chemical state with Co addition, suggesting a consistent metal site filling. To further probe the chemical state of Co found in pentlandite, CTM4XAS was used to simulate the XPS spectra of excited states. Co was found to be associated with a 2 + oxidation state through simulation and is consistent with observations for Fe and Ni XPS spectra, in this study. This links all the transition metals with the dominant tetrahedral metal sites in the crystal structure which have been previously suggested to be in the 2+ oxidation states (Pettifer et al., 2020; Legrand et al., 2005; Tenailleau et al., 2006). Therefore, it is likely that in synthetic cobalt pentlandites Co undergoes the same equal filling of metal sites alongside Fe and Ni. This can also be used to suggest the most likely spin state for these transition metals. Transition metals in tetrahedral co-ordination generally have much smaller crystal field splitting energies compared to those in octahedral coordination (Vaughan, 1978). Therefore, for these transition metals it is likely that they exist in high-spin states as the electron pairing energy is likely greater than the crystal field splitting energy. If a low-spin state were observed, it would be most evident for iron as octahedral low-spin iron configurations have a set of filled t_{2g} orbitals with no multiplet effects. This high spin state present at tetrahedral metal sites in pentlandite has previously been suggested by Tenailleau et al. (Tenailleau et al., 2006).

4.2. Surface sulfur contributions

Sulfur 2*p* XPS spectra are more sensitive to discrete changes in the surface electronic structure compared to the transition metal 2*p* spectra due to narrower linewidths and final state contributions. The FWHM of all bulk and surface S 2*p* components decreased as a function of Co. Metal sites are occupied by either of Fe or Ni, each with different bond lengths and electron densities. Therefore, these three contributions would create a series of very close but individual peaks to give each of the bulk 5-coordinated, bulk 4-coordinated, and surface 3-coordinated sulfur components in the sulfur 2*p* spectra. The decrease in the FWHM of S 2p is then a result of the samples moving towards having a single discrete crystallographic site as the concentration of Co increases.

All sulfur 2*p* components experience an increase in binding energy as the Co concentration increases in the sample. The bulk 5 coordinated and surface 3 coordinated components experience similar binding energy shifts of approx. 0.2 eV between end members while the 4 coordinated bulk/surface component experience a smaller binding energy shift of 0.07 eV. Further investigation requires atomic resolution to separate individual crystal domains in the polycrystalline sample. The occurrence of the surface components has previously been suggested as a feature of the loss of at least one bonding partner for bulk S species (Pettifer et al., 2020). However similar changes in chemical state may indicate the loss of 2 bonding partners upon fracture for bulk 5 coordinated sulfur to become surface 3 coordinated sulfur.

4.3. Sulfur tail

The ligand to metal charge transfer feature has previously been suggested to result from S 3p and Fe 3d overlapping states in the pentlandite XPS S 2*p* spectra as a high binding energy tail (Pettifer et al., 2020). As the cobalt concentration of pentlandite increased, the area of the tail shape began to decrease (see Section 3.3.3). This suggests that this ligand to metal charge transfer feature is less likely to occur for increasing concentrations of Co. The Co is the only transition metal simulated with a negative charge transfer energy and thus is more likely

Table 8
Co 2*p* Simulation parameters used in CTM4XAS to provide the highest accuracy simulations.

	Slater Integral Reduction			Spin-Orbit Coupling Reduction		Crystal Field Parameters	Charge Transfer Parameters				
Spectra	F_{dd}	F_{pd}	G_{pd}	Core	Valence	10Dq (O_h)	Δ	U_{dd}	U_{pd}	$T(e_g)$	$T(t_{2g})$
Co (2 +) 2*p*	1	1	0.7	1	0	−1	−2.5	3	4	1	2

Table 9
Ni 2*p*Simulation parameters used in CTM4XAS to provide the highest accuracy simulations.

	Slater Integral Reduction			Spin-Orbit Coupling Reduction		Crystal Field Parameters	Charge Transfer Parameters				
Spectra	F_{dd}	F_{pd}	G_{pd}	Core	Valence	10Dq (O_h)	Δ	U_{dd}	U_{pd}	$T(e_g)$	$T(t_{2g})$
Ni (2 +) 2*p*	1	1	0.8	1	0	−1	2	4	5	1.2	2.4

to be in the stable $3d^8\underline{L}$ initial state for photoemission. Therefore, ligand to metal charge transfer occurs in different vacant states during the photoemission process than would be seen for Fe, which reduces the likelihood of ligand to metal charge transfer.

5. Conclusion

This study has been able to reproducibly synthesise pure and homogenous cobalt pentlandite samples of $Fe_{4.85}Ni_{4.64}S_8$, $Co_{0.13}Fe_{4.68}Ni_{4.71}S_8$, $Co_{2.73}Fe_{3.13}Ni_{3.16}S_8$, $Co_{5.80}Fe_{1.63}Ni_{1.59}S_8$ and $Co_{8.70}S_8$ stoichiometries. The addition of cobalt was found to decrease the bond length and hence decrease the unit cell dimensions of the cobalt pentlandite crystal structure by up to 0.18 Å (1.8%). The binding energies for the bulk 5-coordinated (162.1 eV) and surface 3-coordinated (160.92 eV) sulfur varied by up to 0.2 eV between the samples, suggesting that these states are linked together because of the bulk 5-coordinate losing two bonding partners upon fracture. There is no preferential occupation of the metal sites by Co as supported by the XPS 2p spectra and CTM4XAS simulations although tetrahedral metal sites dominate photoemission spectra. These tetrahedral metal sites are found to be occupied by transition metals in a high-spin 2 + oxidation state, in line with the 65-electron rule established previously for pentlandites. Finally, ligand to metal charge transfer was less likely to occur with increasing Co content, as evidenced by the decreasing tail in the fitted sulfur 2*p* spectra, supporting that the charge transfer tail is associated with the Fe-S overlapping states.

Role of the funding source

The funding source was not involved in the conduct of the research and/or the preparation of the article.

CRediT authorship contribution statement

Reece R. Waltrovitz: Methodology, Software, Validation, Formal analysis, Investigation, Data curation, Writing – original draft. **Gujie Qian:** Methodology, Formal analysis, Resources, Writing – review & editing. **Frank de Groot:** Software, Validation, Formal analysis. **Jamie S. Quinton:** Writing – review & editing, Supervision. **Sarah L. Harmer:** Conceptualization, Methodology, Validation, Resources, Writing – review & editing, Supervision, Project administration, Funding acquisition.

Declaration of Competing Interest

The authors declare the following financial interests/personal relationships which may be considered as potential competing interests: Sarah Harmer reports financial support was provided by Australian Research Council.

Data availability

Data will be made available on request.

Acknowledgements

This work was supported by the Australian Research Council through FT110100099. We are grateful for access to the Kratos AXIS Ultra DLD XPS spectrometer at The University of South Australia, as well as the Flinders Microscopy and Microanalysis XRD and SEM facilities. We thank Mr Chris Bassell and Dr Alex Sibley for instrument training and technical expertise with data acquisition at each location.

References

Al-Mamun, M., Wang, Y., Liu, P., Zhong, Y.L., Yin, H., Su, X., Zhang, H., Yang, H., Wang, D., Tang, Z., 2016. One-step solid phase synthesis of a highly efficient and robust cobalt pentlandite electrocatalyst for the oxygen evolution reaction. J. Mater. Chem. A 4, 18314–18321.

Biesinger, M.C., 2022. Accessing the robustness of adventitious carbon for charge referencing (correction) purposes in XPS analysis: Insights from a multi-user facility data review. Appl. Surf. Sci. 597, 153681.

Biesinger, M.C., Payne, B.P., Grosvenor, A.P., Lau, L.W.M., Gerson, A.R., Smart, R.S.C., 2011. Resolving surface chemical states in XPS analysis of first row transition metals, oxides and hydroxides: Cr, Mn, Fe, Co and Ni. Appl. Surf. Sci. 257, 2717–2730.

Burdett, J.K., Miller, G.J., 1987. Polyhedral clusters in solids. Electronic structure of pentlandite. J. Am. Chem. Soc. 109, 4081–4091.

de Groot, F., 2005. Multiplet effects in X-ray spectroscopy. Coord. Chem. Rev. 249, 31–63.

De Groot, F., Kotani, A., 2008. Core level spectroscopy of solids. CRC Press.

Department for Energy and Mining, Nickel, in, Government South Australia, 2020.

Fairley, N., 2010. CasaXPS, in. Casa Software Ltd., Teignmouth, UK.

Hoffman, G.G., Bashkin, J.K., Karplus, M., 1990. Electronic structure of icosahedral cobalt-sulfur clusters. J. Am. Chem. Soc. 112, 8705–8714.

Ikeno, H., de Groot, F.M., Stavitski, E., Tanaka, I., 2009. Multiplet calculations of L2, 3 x-ray absorption near-edge structures for 3d transition-metal compounds. J. Phys.: Condens. Matter 21, 104208.

Johansson, G., Hedman, J., Berndtsson, A., Klasson, M., Nilsson, R., 1973. Calibration of electron spectra. J. Electron Spectrosc. Relat. Phenom. 2, 295–317.

Kaneda, H., Takenouchi, S., Shoji, T., 1986. Stability of pentlandite in the Fe-Ni-Co-S system. Miner. Deposita 21, 169–180.

B. Konkena, K. junge Puring, I. Sinev, S. Piontek, O. Khavryuchenko, J.P. Dürholt, R. Schmid, H. Tüysüz, M. Muhler, W. Schuhmann, U.-P. Apfel, Pentlandite rocks as sustainable and stable efficient electrocatalysts for hydrogen generation, Nature Communications, 7 (2016) 12269.

Kouvo, O., Huhma, M., Vuorelainen, Y., 1959. A natural cobalt analogue of pentlandite, in. Mineralogical Society of America.

Legrand, D., Bancroft, G., Nesbitt, H., 1997. Surface characterization of pentlandite,(Fe, Ni) 9S8, by X-ray photoelectron spectroscopy. Int. J. Miner. Process. 51, 217–228.

Legrand, D., Bancroft, G., Nesbitt, H., 2005. Oxidation/alteration of pentlandite and pyrrhotite surfaces at pH 9.3: Part 1. Assignment of XPS spectra and chemical trends. Am. Mineral. 90, 1042–1054.

Malysiak, V., Shackleton, N., O'Connor, C., 2004. An investigation into the floatability of a pentlandite–pyroxene system. Int. J. Miner. Process. 74, 251–262.

Mkhonto, P., Chauke, H., Ngoepe, P., 2015. Ab initio Studies of O2 Adsorption on (110) Nickel-Rich Pentlandite (Fe4Ni5S8) Mineral Surface. Minerals 5, 665–678.

Momma, K., Izumi, F., 2011. VESTA 3 for three-dimensional visualization of crystal, volumetric and morphology data. J. Appl. Crystallogr. 44, 1272–1276.

Moulder, J.F., 1995. Handbook of X-ray photoelectron spectroscopy. Phys. Electron. 230–232.

Pearson, A.D., Buerger, M., 1956. Confirmation of the crystal structure of pentlandite, in. Mineralogical Society of America.

Pettifer, Z.E., Quinton, J.S., Skinner, W.M., Harmer, S.L., 2020. New interpretation and approach to curve fitting synchrotron X-ray photoelectron spectra of (Fe, Ni)9S8 fracture surfaces. Appl. Surface Sci. 504, 144458.

Rajamani, V., Prewitt, C., 1975. Thermal expansion of the pentlandite structure. Am. Mineral.: J. Earth Planet. Mater. 60, 39–48.

Ramanantoanina, H., Daul, C., 2017. A non-empirical calculation of 2p core-electron excitation in compounds with 3d transition metal ions using ligand-field and density functional theory (LFDFT). PCCP 19, 20919–20929.

Richardson, S., Vaughan, D., 1989. Surface alteration of pentlandite and spectroscopic evidence for secondary violarite formation. Mineral. Mag. 53, 213–222.

Shirley, D.A., 1972. High-resolution X-ray photoemission spectrum of the valence bands of gold. Phys. Rev. B 5, 4709.

Smialkowski, M., Tetzlaff, D., Hensgen, L., Siegmund, D., Apfel, U.-P., 2021. Fe/Co and Ni/Co-pentlandite type electrocatalysts for the hydrogen evolution reaction. Chin. J. Catal. 42, 1360–1369.

Stavitski, E., de Groot, F.M., 2010. The CTM4XAS program for EELS and XAS spectral shape analysis of transition metal L edges. Micron 41, 687–694.

Stetina, T.F., Kasper, J.M., Li, X., 2019. Modeling L2, 3-edge X-ray absorption spectroscopy with linear response exact two-component relativistic time-dependent density functional theory. J. Chem. Phys. 150, 234103.

Tenailleau, C., Etschmann, B., Ibberson, R.M., Pring, A., 2006. A neutron powder diffraction study of Fe and Ni distributions in synthetic pentlandite and violarite using 60Ni isotope. Am. Mineral. 91, 1442–1447.

Tsukimura, K., Nakazawa, H., Endo, T., Fukunaga, O., 1992. Cation distribution in pentlandites (Fe, Ni) 9 S 8: Dependence on pressure and temperature and kinetics of the cation exchange reaction. Phys. Chem. Miner. 19, 203–212.

Vaughan, D.J., 1978. Mineral chemistry of metal sulfides, Cambridge Earth Sci. Ser., Cambridge 493.

Xia, F., Zhou, J., Brugger, J., Ngothai, Y., O'Neill, B., Chen, G., Pring, A., 2008. Novel route to synthesize complex metal sulfides: hydrothermal coupled dissolution−reprecipitation replacement reactions. Chem. Mater. 20, 2809–2817.